Phase transformation mechanisms occurring during spark plasma sintering elaboration of new duplex composite stainless steels

R. Mvodo Eba, Maria-Rosa Ardigo-Besnard, J.-P. Chateau-Cornu, F. Herbst, N. Geoffroy, A. Besnard, C. Vandenabeele, S. Lucas, A. Descamps-Mandine, C. Josse

Materials Chemistry and Physics 325 (2024) 129796

Contents lists available at ScienceDirect

Materials Chemistry and Physics

journal homepage: www.elsevier.com/locate/matchemphys

Phase transformation mechanisms occurring during spark plasma sintering elaboration of new duplex composite stainless steels

R. Mvodo Eba [a,*], M.R. Ardigo-Besnard [a], J.-P. Chateau-Cornu [a], F. Herbst [a], N. Geoffroy [a], A. Besnard [b], C. Vandenabeele [c], S. Lucas [c,d], A. Descamps-Mandine [e], C. Josse [e]

[a] Laboratoire Interdisciplinaire Carnot de Bourgogne (ICB), UMR 6303 CNRS, Univ. Bourgogne, BP 47870, 21078, DIJON, Cedex, France
[b] Arts et Metiers Institute of Technology, LaBoMaP, Univ. Bourgogne Franche-Comté, 71250, Cluny, France
[c] Innovative Coating Solutions, 11 Place Saint Pierre, 5380, Forville, Belgium
[d] Laboratoire d'Analyse par Réactions Nucléaires (LARN), Namur Institute of Structured Matter (NISM), University of Namur, 61 Rue de Bruxelles, 5000, Namur, Belgium
[e] Centre de Microcaractérisation Raimond Castaing (CNRS UAR 3623), Espace Clement Ader, 3 rue Caroline Aigle, 31400, Toulouse, France

HIGHLIGHTS

- New composite duplex stainless steels were developed by spark plasma sintering.
- Different mass fractions of austenitic and ferritic powders were blended.
- Martensite forms at the austenite/ferrite interfaces in sintered steels.
- Chromium and nickel diffusion affect the width of the martensitic regions.
- The size of ferritic and austenitic domains corresponds to powders' particles size.

ARTICLE INFO

Keywords:
Powder metallurgy
Duplex stainless steels
Spark plasma sintering
Phase transformation

ABSTRACT

This study focuses on the elaboration of duplex stainless steels (DSS) from powder mixtures using spark plasma sintering (SPS). Different mass fractions of an austenitic 316L powder and a ferritic 410L one were blended and then sintered by SPS. Microstructural characterizations of the sintered samples obtained from different powder mixtures were performed. They were coupled with marking experiments of the powder particles' surface. The results showed the formation of martensite within the ferritic powder and at the austenite/ferrite interfaces, following two different mechanisms. In addition, it was found that the width of the martensitic regions is mainly influenced by the diffusion of Cr and Ni from the austenitic to the ferritic powder during sintering. The characterizations revealed that the originality of this approach lies in the particular microstructure obtained after sintering. The characteristic size of the ferritic and austenitic domains in the final material is that of the initial powder particles (up to some hundred microns). Moreover, each domain is formed by equiaxed and isotropic grains, having a size ranging from some microns to some tens of microns. This particular microstructure justifies the use of the term "composite duplex stainless steels" (COMPLEX) for this kind of new DSS.

1. Introduction

In 1927, Bain and Griffiths documented the discovery of a duplex microstructure in iron-chromium-nickel alloys [1]. The first duplex stainless steels (DSS) were elaborated in 1930 in Sweden and used in the sulfite paper industry [2–5]. These steels were developed to address intergranular corrosion issues, commonly encountered in high-carbon austenitic steels [2,3]. Contemporary DSS exhibit a mixed microstructure with approximately equal volume fractions of ferrite and austenite. This particular microstructure combines the advantages of both austenitic and ferritic stainless steels, thus creating a corrosion-resistant material while providing excellent mechanical strength [3,4,6,7]. The lower content of costly nickel in DSS compared to austenitic steels offers similar protection against pitting and crevice corrosion [4,6,8]. Thanks

* Corresponding author.
E-mail address: reine.mvodo-eba@u-bourgogne.fr (R. Mvodo Eba).

https://doi.org/10.1016/j.matchemphys.2024.129796
Received 28 May 2024; Received in revised form 19 July 2024; Accepted 1 August 2024
Available online 5 August 2024

to the well-balanced mechanical properties, corrosion resistance, and economic advantages compared to austenitic stainless steels, the use of DSS in the industry has increased since their discovery. DSS are widely used in many marine and petrochemical applications due to their high resistance to chloride-induced corrosion [4,8]. They are also found in the nuclear, oil and gas, chemical processes, mineral processing, civil and structural engineering industries [4,9]. The manufacturing of DSS with conventional methods such as forging or rolling, requires a tight control of the chemical composition and the temperature. Indeed, phase transformations occurring in DSS can give rise to undesirable brittle phases such as sigma phase, chromium carbides, and nitrides, which can decrease the ductility and the corrosion resistance [3,7,8]. Powder metallurgy (PM) processes, especially pressure-assisted sintering techniques such as spark plasma sintering (SPS) and hot isostatic pressing (HIP), represent alternative and innovative methods for the development of new materials with controlled microstructure and chemical composition. One strategy consists, for example, in mixing powders of different natures to independently control the chemical composition and phase proportions in the final material [10,11]. This is not achievable with conventional elaboration methods. In such techniques the phase equilibrium diagram and the lever rule impose a relationship between the chemical composition and phase proportions in a solid material. The homogenous and fine microstructures achieved through PM manufacturing processes contribute to improving the properties of the final material [12]. Moreover, pressure-assisted sintering techniques allow the elaboration of near-net-shape parts, even with complex shapes. In addition, due to the high heating and cooling rates achieved especially during SPS [13], the precipitation of brittle phases (sigma phase, carbides, and nitrides) can often be reduced [12,14,15].

Different approaches are reported in the literature to elaborate DSS from metal powders. Dobrzanski et al. [16] used, as starting materials, 316L or 410L powders mixed with varying amounts of pure elements such as Ni, Mo, and Cu. The blends were sintered in a vacuum furnace with argon backfilling at 1260 °C for 1 h. They compared the results to those obtained from a blend of 410L and 316L in a 1:1 ratio. They found that the addition of pure elements in the blends leads to lower mechanical properties compared to DSS obtained by mixing a ferritic and an austenitic powder in equal fractions. Other authors sintered mixtures of ferritic and austenitic powders by pressure-assisted sintering techniques such as SPS [17,18], HIP [17,19,20], and field-assisted hot pressing (FAHP) [12]. They all observed, after sintering, the formation of a fine martensite-like microstructure at the austenite/ferrite interfaces. Because of the elementary diffusion due to the use of powders of different chemical compositions, this fine microstructure presents a varying chemical composition [12,17–20]. Finally, Ardigo-Besnard et al. [21] obtained an austenitic-ferritic stainless steel starting from 316L powders coated by a thin chromium layer deposited by physical vapor deposition (PVD) technique and then consolidated by SPS.

In the present study, SPS was used to elaborate DSS by mixing austenitic 316L and ferritic 410L powders, whose mass fractions range from 10 to 90 %. The selection of SPS as the manufacturing method was motivated by the possibility of elaborating samples in a time-efficient manner due to its rapid heating and cooling rates. Moreover, the formation of undesired phases is limited. Diffusion mechanisms and phase transformations occurring during sintering were investigated and correlated to the final observed microstructures. In addition, an innovative approach based on the use of marked 410L powder particles has been employed to identify the initial austenite/ferrite interfaces.

2. Materials and methods

2.1. Raw materials and sintering conditions

The austenitic 316L and ferritic 410L powders were supplied by Aubert & Duval and MP Tech International, respectively. They were both produced by argon atomization. Their chemical composition is reported in Table 1. Particle size ranges from 0 up to 500 μm for the 316L powder, and from 45 up to 150 μm for the 410L one.

Table 1
Chemical composition of 316L and 410L powders.

Element (wt. %)	C	Cr	Ni	Mo	Mn	Si	O	Fe
316L	<0.02	17.7	11.9	2.44	1.88	0.83	0.02	Bal.
410L	<0.02	12.6	0.17	–	0.28	0.35	<0.01	Bal.

Table 2
Mass fractions of powder mixtures.

	Mass fraction (%)						
410L	0	10	25	50	75	90	100
316L	100	90	75	50	25	10	0
ID sample	0–100	10–90	25–75	50–50	75–25	90–10	100–0

The powders were sintered using an HPD-125 apparatus (FCT Systeme GmbH). Powders were consolidated under vacuum (0.3 mbar), using a cylindrical graphite die with an inner diameter of 60 mm. The obtained cylindrical pellets were 10 mm in height. The sintering process was performed with a heating rate of 50 °C/min from the ambient temperature up to 1100 °C. The heating step was followed by a dwell time of 15 min at 1100 °C, and a holding pressure of 70 MPa. The samples were naturally cooled (approximately 40 °C.min^{-1} from 1100 down to 600 °C and 20C min^{-1} from 600 down to 400 °C). Firstly, the austenitic and ferritic powders were individually sintered. Then, five powder mixtures containing different austenite/ferrite mass fractions, as indicated in Table 2, were prepared. The powders underwent an 8-h mixing process in a Turbula© mixer before sintering. This process ensures homogenization and prevent particle agglomeration which is known to hinder densification during the sintering [22].

The sintered samples were cut into pieces of 10 mm × 10 mm x 5 mm for X-ray diffraction (XRD), hardness measurements, and microstructural observations. Square bars of 20 mm × 5 mm x 5 mm were core-cut for dilatometric tests. For microstructural observations, the powders and the sintered samples were polished with SiC papers (down to 1200 grit), diamond paste (down to 1 μm), and colloidal silica (0.03 μm). Additional superfinishing steps were performed with vibratory polishing for 4 h using the Buehler Vibromet 2, followed by 15 min of ionic polishing using the Hitachi IM4000.

2.2. Characterization methods

Phase identification in powders and sintered samples was performed by X-ray diffraction (XRD) using a Bruker D8-A25 diffractometer with Cu Kα radiation (λ = 0.154056 nm). Phase quantification was performed by the Rietveld method. Microstructural examinations of both powders and sintered samples were conducted using a JEOL JSM-7600F scanning electron microscope (SEM) equipped with a field emission gun (FEG) and coupled with an energy-dispersive X-ray spectrometer (EDS). Elemental EDS analyses and profiles were performed at 15 kV. Phase and orientation maps were generated by electron backscattered diffraction (EBSD) analyses. EBSD measurements were carried out with a JEOL JSM-7600F SEM with an accelerating voltage of 20 kV. The SEM was coupled with an EDAX-TSL acquisition system featuring a Digiview V camera. Transmission electron microscopy (TEM) was used to characterize the microstructures of samples at the nanometric scale. A thin cross-section was taken from a sintered sample by focused ion beam (FIB), using a Thermo Fischer HeliosNanoLab 600i apparatus and gallium ions. TEM characterizations were performed with a JEOL JEM-2100F operating at an accelerating voltage of 200 kV.

Phase transformations were investigated through dilatometry tests. The sintered samples were heated up to 1100 °C, held at this temperature for 20 min, and then cooled at a rate of 16 °C/min. The dilatometer

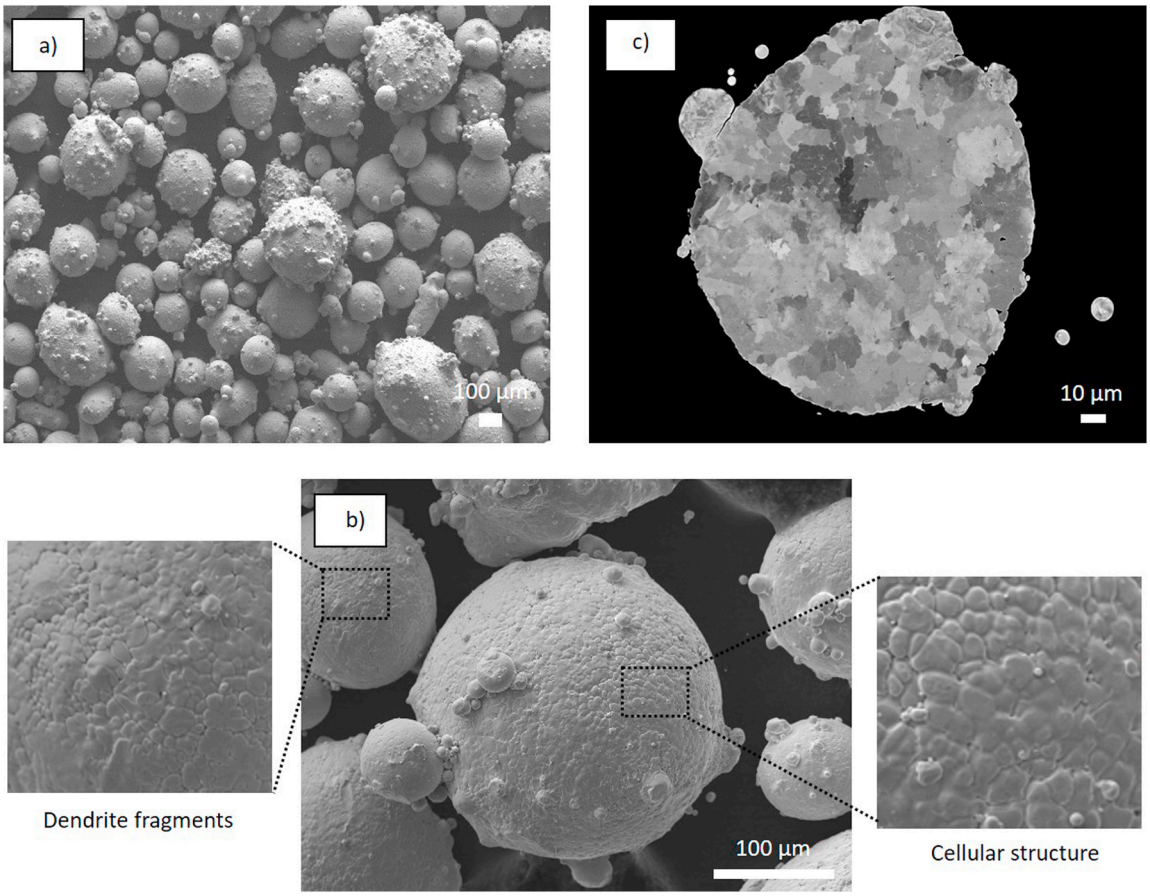

Fig. 1. 316L powder particles: (a)–(b) backscattered electron images; (c) cross section.

used was a L75 platinum series supplied by Linseis. Data processing was carried out with Linseis TA evaluation software.

Tantalum coating on 410L powder particles was synthesized by a DC magnetron sputtering system using a circular (50.8 mm in diameter, 6 mm thick) tantalum metallic target (purity 99.99 %). The powder was continuously stirred in a dedicated reactor during deposition to ensure a complete covering of each individual particle. Before deposition, the chamber was pumped down to reach a residual pressure of $3.5 \bullet 10^{-3}$ Pa. A DC Ar etching was performed at 3 Pa, and the deposition took place at 1.3 Pa to achieve an expected film thickness of around 80 nm.

3. Results and discussion

3.1. Powders characterizations before sintering

3.1.1. 316L

316L powder particles are almost spherical, as shown in Fig. 1 (a). A significant number of satellites can be observed mainly on larger particles' surface. These satellites are the results of the collisions between partially solidified particles in the spray chamber during the atomization process [23–26]. Fritsching [27] and Achelis et al. [28] explained that these satellite particles are due to the re-circulation of fine particles

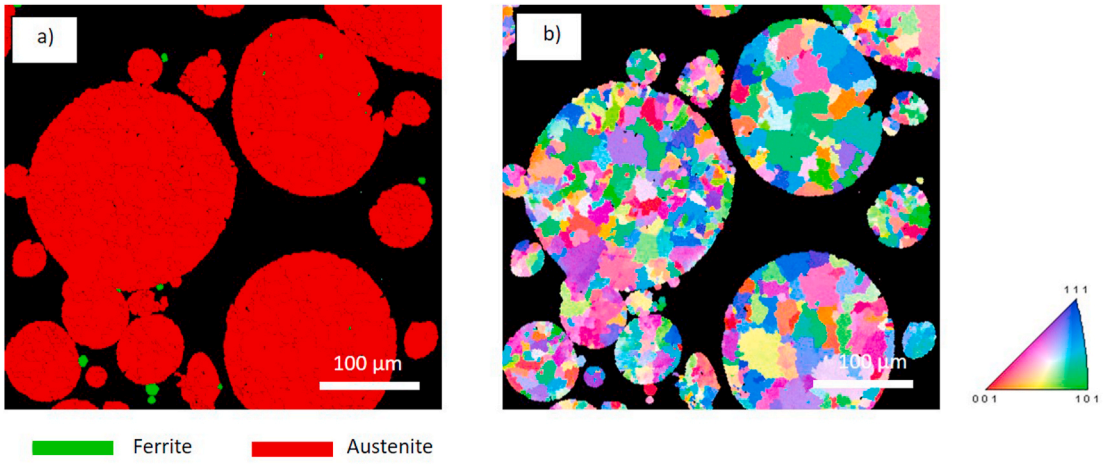

Fig. 2. EBSD maps of 316L powder particles: (a) phases and (b) orientations.

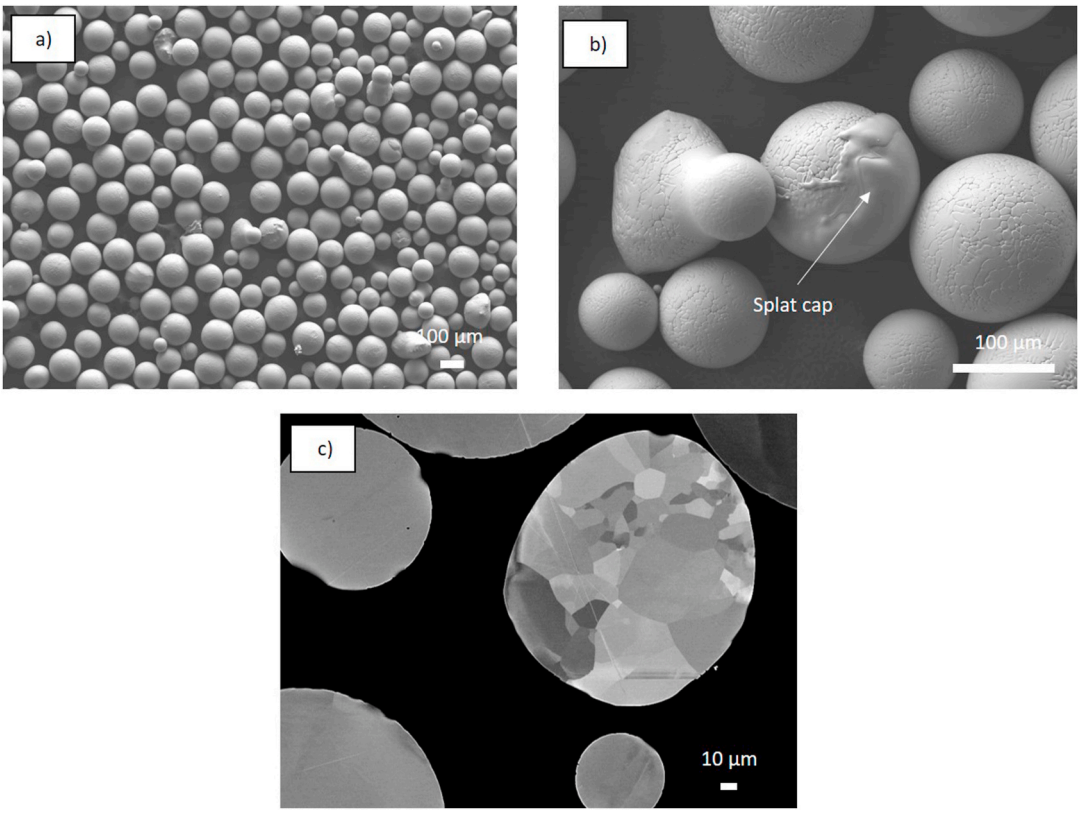

Fig. 3. 410L powder particles: (a)–(b) backscattered electron images; (c) cross section.

within the gas streams inside the spray chamber, promoting particle contact through surface tension. It is reported in the literature that satellite particles negatively impact the compactness and flow of powders [25,29,30].

At the microstructural level, the 316L powder presents a cellular and a so-called "dendrite fragments" structure [31] (Fig. 1 (b)). The cellular structure can be easily identified in the cross-section observation (Fig. 1 (c)). The microstructure of the powders strongly depends on the atomization process, the nature of the heterogeneous nucleation in the molten metal, and the subcooling of the droplets [31,32]. Grgač et al. [31] studied the microstructure of a Ch12MF4 steel (2.37 wt% C, 12.06 wt% Cr, 1.2 wt% Mo and 4.0 wt% V) during non-equilibrium solidification of liquid metal drops. They found that the final microstructure is determined by the thermodynamic and thermokinetic conditions during cooling. The dendritic microstructure would result from rapid cooling, while during slow cooling the cellular microstructure is favored. On the contrary, Pengjun et al. [23] demonstrated that during gas atomization (using argon and nitrogen) of a nickel-based superalloy, a cellular microstructure is favored when rapid cooling rates are employed. Similarly, Kumar et al. [33] observed that in a Ni-based superalloy a cellular microstructure is obtained for small-sized grains where heat transfer is rapid, resulting in a fast cooling rate. Although the formation of cellular and "dendrite fragments" structures remains controversial, it is evident that the variations in morphology and microstructure observed within 316L powder particles are directly influenced by the atomization process.

The XRD analysis carried out on the 316L powder (see supplementary materials S1) reveals that it contains 97 % austenite (face-centered cubic structure, f.c.c.; PDF 04-002-1864) and 3 % residual ferrite (body-centered cubic structure, b.c.c.; PDF 04-004-6353), which is typical of 316 steels. The EBSD phase map (Fig. 2 (a)) confirms these results. The EBSD orientation map (Fig. 2 (b)) shows polycrystalline particles with

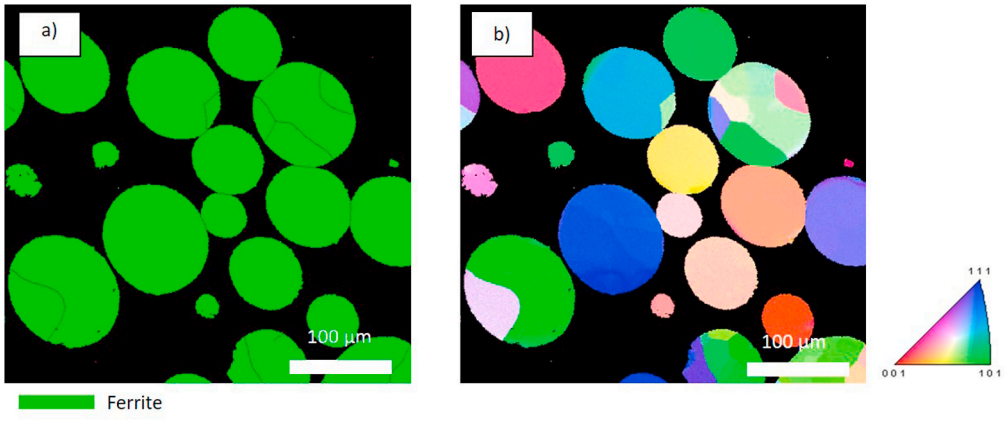

Fig. 4. EBSD maps of 410L powder particles: (a) phases and (b) orientations.

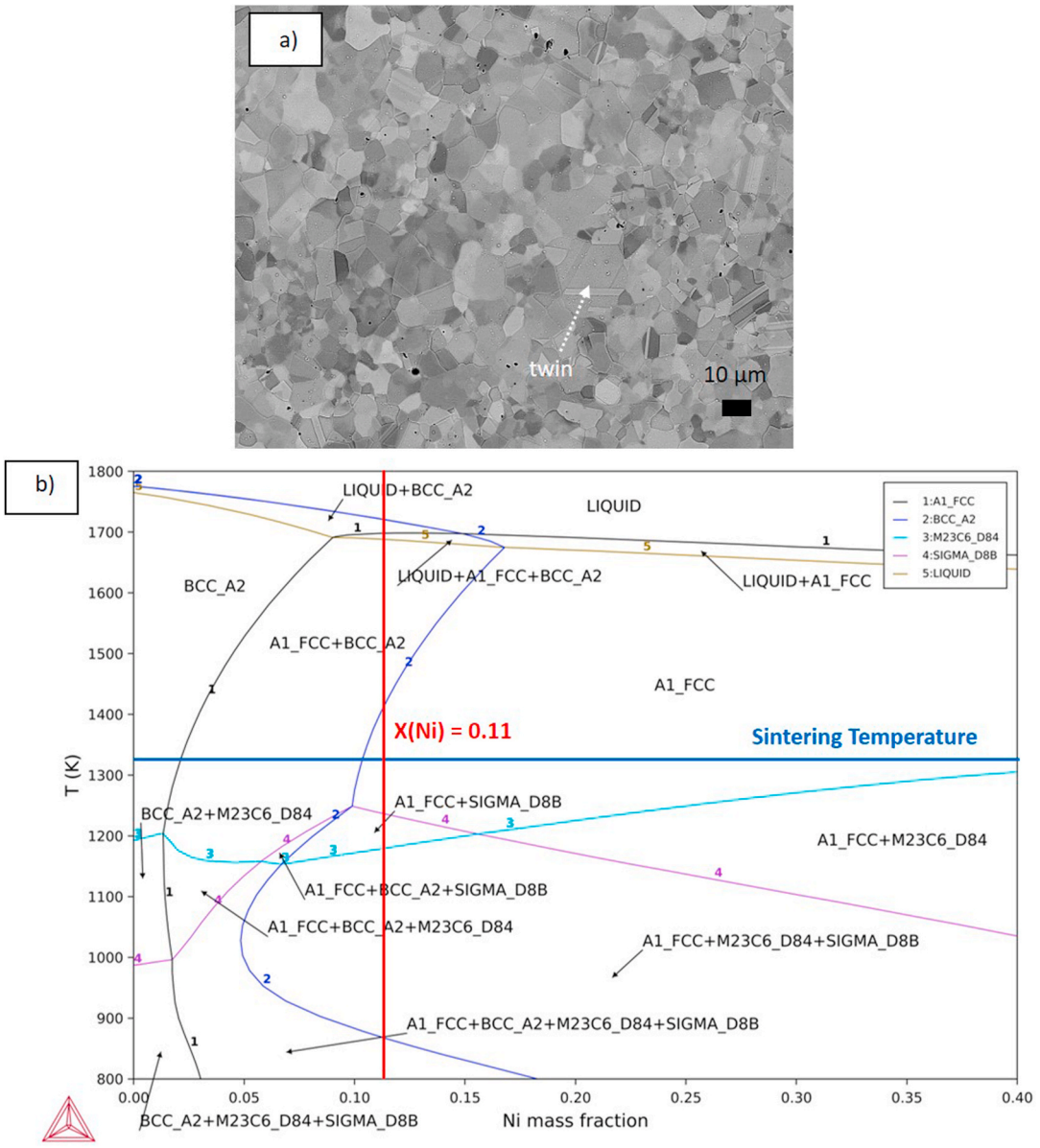

Fig. 5. (a) Core-microstructure of sintered 316L; (b) calculated isopleth section of 316L in function of Ni mass-fraction obtained with Thermo-Calc software (version 2022a), using TCFE12 (Thermo-Calc steel and Fe-alloys) database.

equiaxed grains and random orientations. A greater grain density is observed in larger particles, due to multiple dendrite nucleation sites, unlike smaller particles [33]. In addition, larger particles present finer grains. According to Kumar et al. [33], this phenomenon can be attributed to a higher probability of dendrite remelting during the recalescence phase. This subsequently leads to their fragmentation and results in grain refinement. Satellite particles exhibit a fine-grained microstructure similar to the particles they are attached to.

3.1.2. 410L

410L powder particles are almost spherical and regular, with a smooth surface (Fig. 3 (a)). The sphericity of particles is influenced by the spherization and solidification time [23]. When the spherization time is shorter than the solidification time, particles tend to adopt a regular shape and a smooth surface, as observed in the present study for the 410L powder [23]. The spherization time t_s (s) is given by Ref. [23]:

$$t_s = (3.\pi..V.\sigma).().^4.\left(d_1^4 - d_2^4\right) \quad (1)$$

where μ_L is the viscosity of the liquid metal (Pa.s), V the volume of the drop (m^3), d_1 and d_2 the diameters of the drop respectively before and after spherization (m) and σ the surface tension of the liquid metal (N. m^{-1}).

This equation illustrates that the spherization time increases with the particles' diameter. Consequently, 410L particles are more likely to have a spherical shape compared to 316L ones. 410L powder particles also contain defects, notably splat-caps (Fig. 3 (b)), which form when a liquid drop spreads on the surface of a particle completely solidified [26,33]. Cross-section observations (Fig. 3 (c)) show that some particles have a cellular microstructure with equiaxed grains, and some others seem to be monocrystalline.

XRD analysis (see supplementary material S1) reveals that the 410L powder is fully ferritic (PDF 04-004-6353). This result is confirmed by the EBSD phase map (Fig. 4 (a)). The EBSD orientation map (Fig. 4 (b)) shows the existence of both monocrystalline and polycrystalline particles with random grain orientations, confirming cross-section observations. Unlike 316L, 410L powder particles have a low grain density. Moreover, these grains are larger compared to the ones observed in the

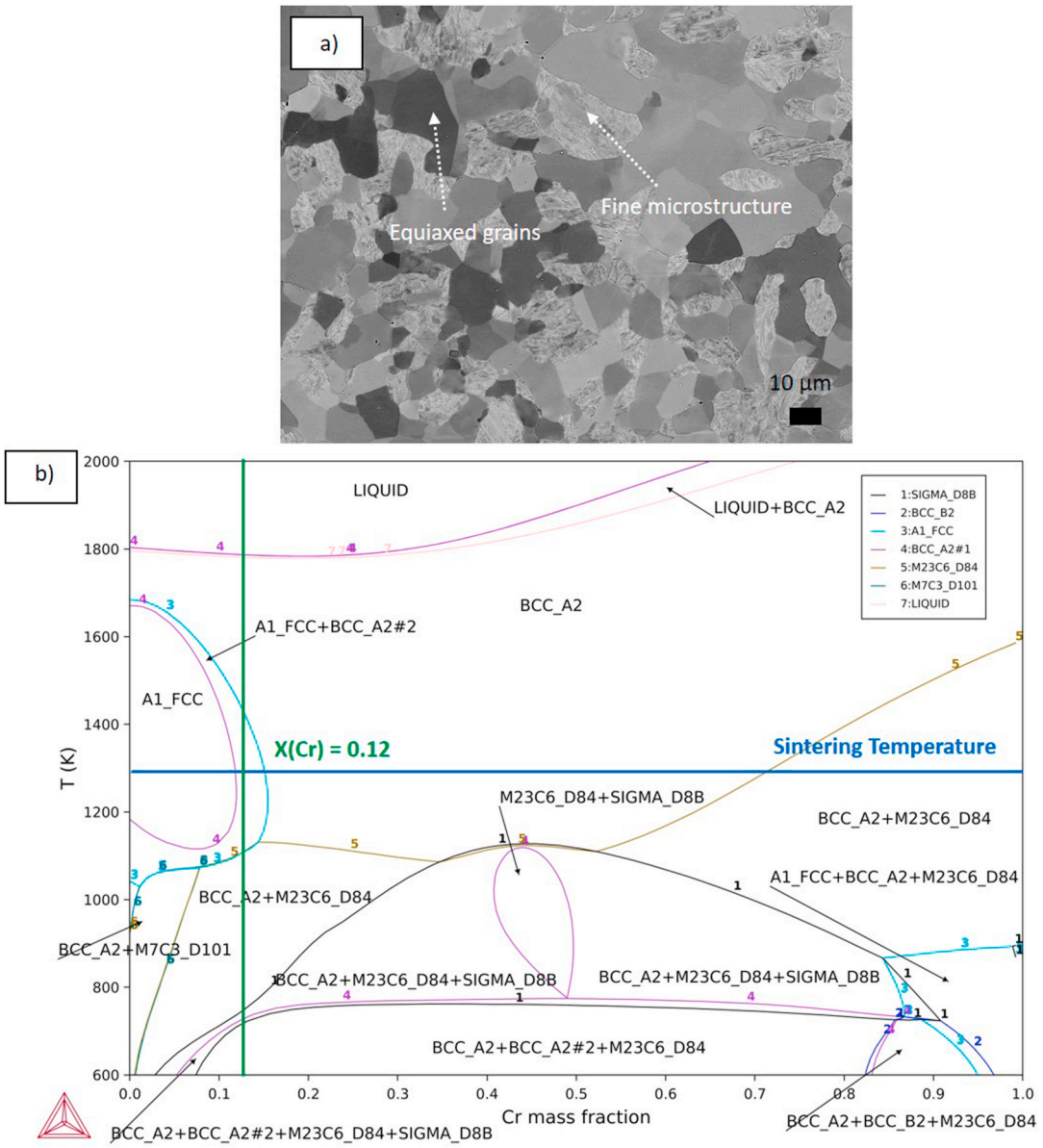

Fig. 6. (a) Core microstructure of sintered 410L; (b) isopleth section of 410L in function of Cr mass-fraction calculated with Thermo-Calc software (version 2022a), using TCFE12 (Thermo-Calc steel and Fe-alloys) database.

316L powder. This microstructure is probably due to the reduced amount of available nucleation sites within the fine particles during the grain formation process [33].

3.2. Individually sintered powders

3.2.1. 316L

The core-microstructure of the sintered 316L is shown in Fig. 5 (a). It is composed of equiaxed grains and twins, as commonly observed for f.c.c. materials. This fine microstructure is in agreement with previous studies performed on 316L elaborated by SPS under similar experimental conditions [34,35]. Moreover, the comparison with these works confirmed that the sintering parameters used in the present study (1100 °C - 75 MPa) ensure optimal densification. The black spots correspond to either porosities or oxides. The XRD analysis (see supplementary material S2) indicates the exclusive presence of austenite (PDF 04-002-1864). On the other hand, the calculated isopleth section of 316L as a function of Ni mass-fraction (Fig. 5 (b)) predicts the presence of mere austenite at the sintering temperature (1100 °C), and of austenite, ferrite, $M_{23}C_6$-type carbides and σ phase below 600 °C. These differences between thermodynamic calculations and experimental results can be attributed to the fact that SPS is a non-equilibrium process. It is reasonable to suppose that the cooling rate during SPS is high enough to preserve at room temperature the f.c.c. phase formed at 1100 °C.

The EBSD phase map confirms the presence of mere austenite with a random grain orientation (see supplementary material S3 (a) phases and (b) orientations).

3.2.2. 410L

The core microstructure of the sintered 410L is composed of a random combination of two different microstructures: coarse equiaxed grains and a finer microstructure (Fig. 6 (a)). XRD indicates that the sample is only composed of a b.c.c. phase (PDF 04-004-6353; see supplementary material S2). Ferritic steels with low carbon content such as 410L are designed to undergo the two-phase transformation, consisting of ferrite and austenite [36]. This is also indicated in the calculated isopleth section of 410L as a function of Cr mass-fraction at the sintering temperature of 1100 °C (Fig. 6 (b)). On the other hand, at 327 °C, the

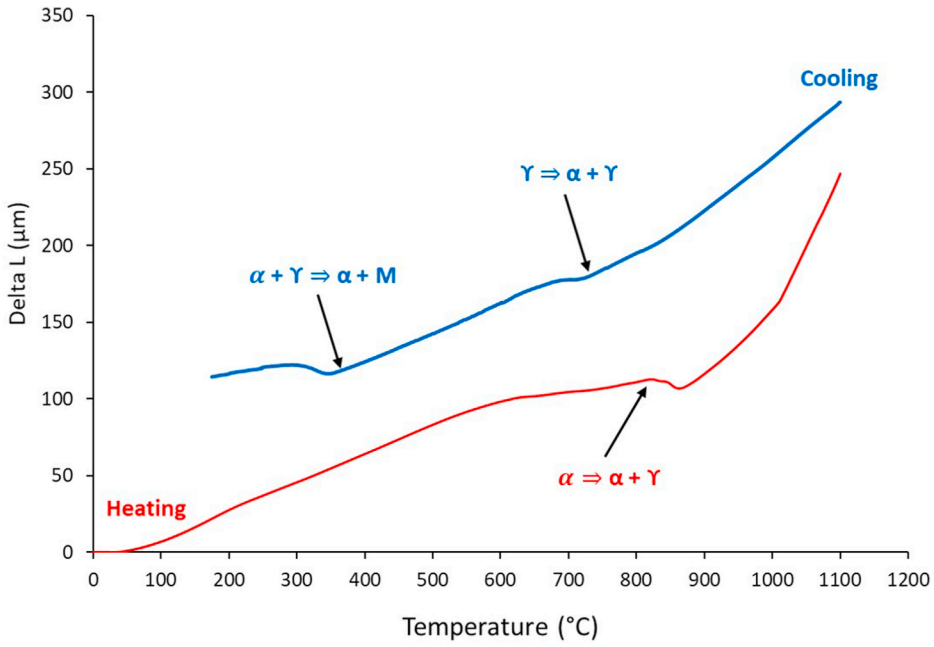

Fig. 7. Dilatometric curve of sintered 410L.

thermodynamic calculations predict the presence of the b.c.c. phase and $M_{23}C_6$-type carbides. This is not in agreement with the XRD results. The possible reasons are the non-equilibrium conditions during sintering or the eventual formation of nanocarbides not detectable at the XRD/SEM scale.

The presence of two different microstructures in the sintered 410L is obviously linked to phase transformations occurring during sintering. To better understand their formation mechanisms, a dilatometric analysis was performed. The results are presented in Fig. 7. During heating, a phase transformation can be observed at about 820 °C. By comparison with the data from the isopleth section (Fig. 6 (b)), this transformation corresponds to a partial austenitization of ferrite. During cooling, two phase transformations are visible: a first one at about 730 °C, corresponding to the austenite to ferrite transformation, and a second one at 350 °C, corresponding to a martensitic transformation of the remaining austenite. Indeed, Dadé et al. [37] performed a dilatometric test on a ferritic steel (0.012 wt% C, 13 wt% Cr, and 1 wt% W) previously HIPed at 1100 °C under 1900 bar with a holding time of 2 h. They observed a martensitic transformation at 330 °C, with a cooling rate of 12 °C.min^{-1}, very close to the one used in the present study of 16 °C.min^{-1}. Therefore, the fine microstructure observed in the sintered 410L in the present case corresponds to martensite.

The distinction between ferrite and martensite is challenging, due to the low degree of tetragonality of martensite in low-carbon steels [38]. This is the reason why XRD exclusively detects the b.c.c. phase in the sintered 410L (see supplementary material S2). However, the distinction between martensite and ferrite in EBSD phase map was performed following the approach reported by Nowell et al. [39] and Vunnam et al. [40], based on the image quality (IQ) parameter. The authors showed that EBSD patterns in martensite are generally of lower quality compared to those in ferrite. As IQ decreases, the areas on the map appear darker, and are typically assigned to martensitic regions. As pointed out by Nowell et al. [39], IQ is a qualitative parameter depending on several variables, including EBSD pattern acquisition parameters. Based on ref. [39and40], the following conditions were used to collect data for map construction: 0 % gain setting, 70° tilt, and standard background subtraction. Moreover, points near grain boundaries were omitted from the analysis to reduce the impact of the generally lower IQ values observed in those areas. Finally, as suggested in Ref. [39], IQ data were smoothed by calculating the average IQ within a kernel of a specified size. This procedure minimizes errors and ensures the best differentiation. EBSD phase map in Fig. 8 (a) is a combination of IQ map and b.c.c. ferrite phase map. The darkest regions (with low IQ values and fine microstructure) correspond to martensite. Opposite, the

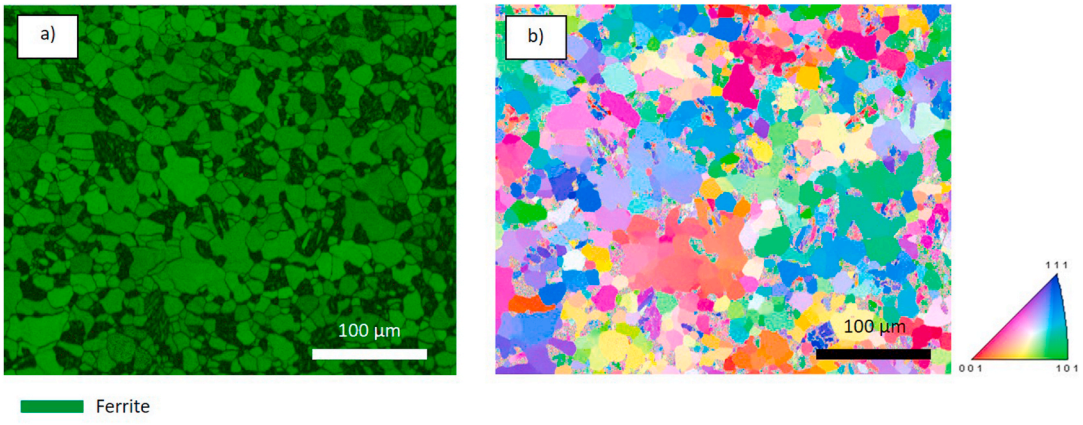

Fig. 8. EBSD maps of sintered 410L: (a) phases and (b) orientations.

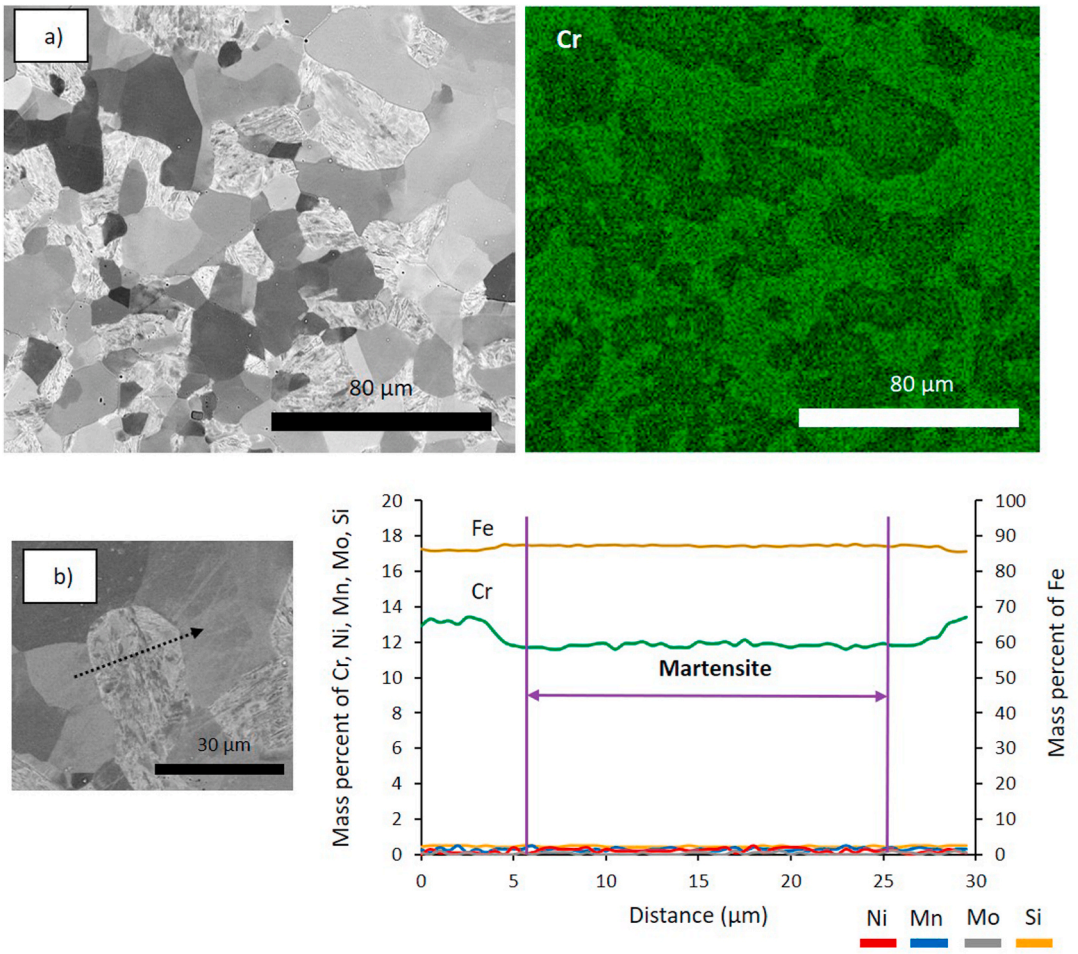

Fig. 9. (a) SEM-EDS Cr map and (b) SEM-EDS elementary profiles in the sintered 410L.

lighter areas (with high IQ values and equiaxed grains) correspond to ferrite. On the other hand, EBSD orientation map (Fig. 8 (b)) shows that both ferrite and martensite grains have a random orientation.

The chromium SEM-EDS mapping of the sintered 410L (Fig. 9 (a)) indicates that the equiaxed regions corresponding to ferrite exhibit a higher Cr content than the finer microstructure corresponding to martensite. The elemental EDS profiles in Fig. 9 (b) display a chromium depletion (approximately 1 wt%) in martensite. At the same time, the distribution of the other alloying elements remains uniform, in agreement with the results reported by Dadé et al. [37]. According to these authors, the partial transformation of ferrite into austenite during heating induces a chemical partitioning of alphagenic elements Cr and W from the transforming ferrite. This phenomenon explains the formation of Cr and W-enriched segregated areas in the final microstructure. Additionally, they attribute the martensite formation to the Cr and W depletion and carbon diffusion (0.012 wt% before HIP and 0.03 wt% after HIP in the matrix), which favors the extension of the austenite + ferrite domain. Auger et al. [41] studied the microstructural transformations of a Fe-14 wt% Cr steel sintered using SPS at 1100 °C under 36 MPa for 4 min. The sample's microstructure consists of equiaxed grains, martensite laths, and chromium precipitates. The authors attributed the formation of martensite to three factors: (i) carbon diffusion from the graphite die, (ii) chromium depletion in the matrix due to the formation of Cr-rich precipitates, and (iii) a rapid cooling rate.

In the present study, core-cut samples (approximately 5 mm from the sample edges in contact with graphite tooling parts) were used to avoid regions in contact with graphite tools, where carbon diffusion effectively leads to carbide formation. Therefore, the formation of martensite cannot be explained by carbon diffusion from graphite tools.

XRD analysis reveals the presence of the mere b.c.c. phase. However, it is generally difficult to detect a phase by XRD when its volume fraction is less than 5 % [42]. To verify the presence of carbides or chromium-rich precipitates in the sintered 410L, TEM analyses were carried out. Fig. 10 (a) shows martensite laths measuring about a hundred nanometers. No carbides or chromium-rich precipitates that could explain the Cr depletion were observed between martensite laths, at the ferrite/martensite interface (Fig. 10 (b)), or in the ferrite phase (Fig. 10 (c)).

A plausible explanation for Cr depletion in martensite formed in the present study is that during partial austenitization occurring during heating, ferrite releases Cr (alphagenic) in favor of the formation of f.c.c. austenite phase. This phase transformation is illustrated by the 410L isopleth section (Fig. 6 (b)). Subsequently, during cooling, this austenite transforms firstly into ferrite at about 730 °C, and the remaining austenite transforms into martensite at 350 °C. The chromium amount of the resulting martensite is inherited from its parent austenite, which is lower than that of the initial ferrite.

As the temperature decreases, the transformation of austenite occurs through a cooperative atomic movement shorter than interatomic distances, resulting in a new crystal structure known as martensite [43,44]. It is a common belief that the germination of martensite is closely associated with a rapid cooling rate, and requires the segregation of carbon to create a carbon-supersaturated solution in deformed α-Fe [44]. 410L steel is classified in the literature within group 1 of ferritic stainless steels (Cr = 10–14 wt%). These steels are known for their capability to undergo a ferrite-to-austenite transformation when heated.

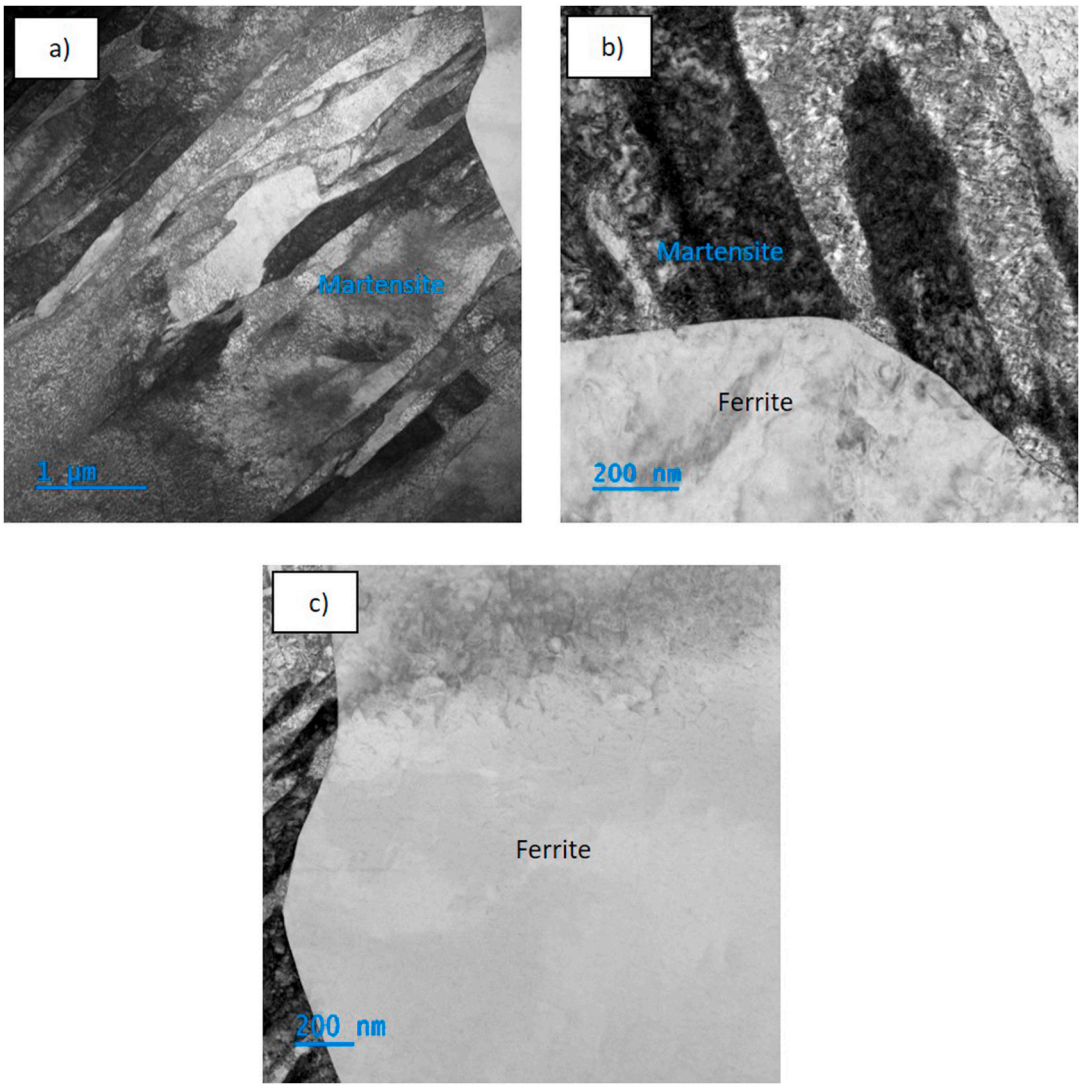

Fig. 10. TEM images of (a) martensite, (b) ferrite/martensite interface and (c) ferrite in sintered 410L.

They also present the possibility of austenite transforming into martensite when rapidly cooled to ambient temperature [45]. In the present study, the martensitic transformation begins at 350 °C (as illustrated in Fig. 7); at this temperature the cooling rate during SPS is 20 °C.min^{-1}. Tsai et al. [46] investigated phase transformations in 410 steel (0.12 wt% C, 12.8 wt% Cr and 0.12 wt% Ni) austenitized at 1100 °C during 10 min and cooled at various cooling rates ranging from 9 °C.min^{-1} up to 600 °C.min^{-1}. Their findings indicate that an increase in the cooling rate primarily lowers the temperature at which martensitic transformation begins (Ms. Nevertheless, they observed that even at the slowest cooling rate of 30 °C.min^{-1} (close to the one measured in the present study), martensite formation occurred. This proves that Ms is not only influenced by the cooling rate, but also by the alloying elements content, following the Andrews formula [47]:

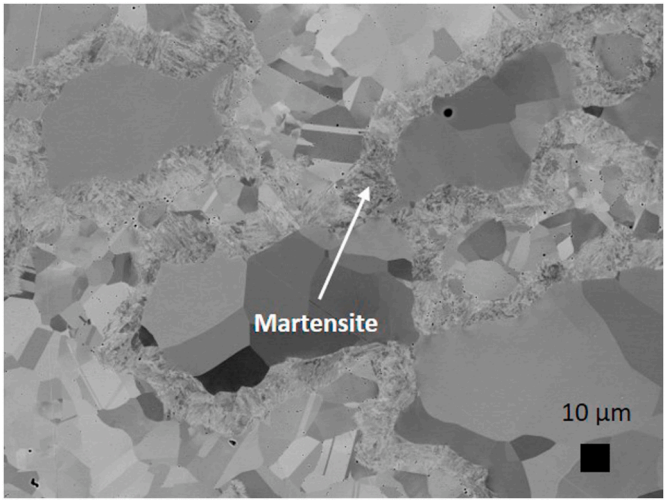

Fig. 11. Core microstructure of 50-50 blend.

$$Ms\ (°C) = 539–423\ (wt.\%\ C) – 17.7\ (wt.\%\ Ni) – 12.1\ (wt.\%\ Cr)$$
$$–7.5\ (wt.\%\ Mo) – 30.4\ (wt.\%\ Mn) \quad (2)$$

Moreover, Zheng et al. [48] studied the microstructure of a low carbon steel (8.39 wt% Cr, 0.093 wt% C and 0.44 wt% Mn) heated at 1350 °C, held at this temperature for 1 min, and cooled at rates ranging from 3600 °C.min^{-1} down to 1 °C.min^{-1}. After a rapid cooling rate of 3600 °C.min^{-1}, the sample exhibits a complete martensitic microstructure. However, at a cooling rate of 60 °C/min and below, ferrite grains begin to form, ultimately resulting in a fully ferritic microstructure at a cooling rate of 1 °C.min^{-1}. Based on these observations, it can be inferred that the SPS conditions used in the present study can lead to

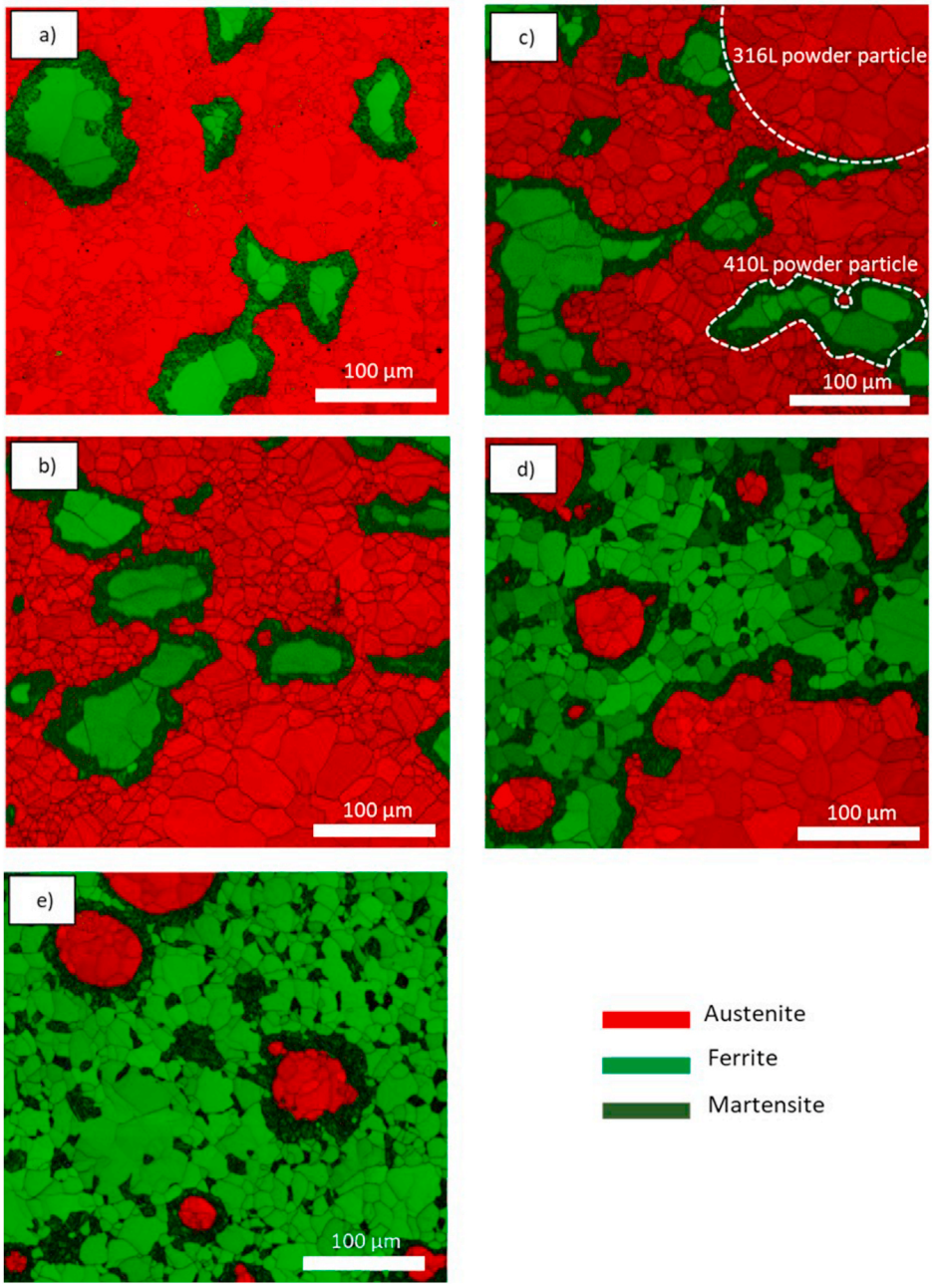

Fig. 12. EBSD phase maps of the five blends: (a) 10–90, (b) 25–75, (c) 50-50, (d) 75-25, and (d) 90-10.

martensite formation in 410L. However, the cooling rate of 20 °C.min^{-1} during SPS does not lead to a fully martensitic microstructure. On the other hand, it is reported in the literature that the martensitic transformation in steels can also be induced by the application of external stress [43]. The role of pressure on martensite formation in the sintered 410L in the present study was investigated via a conventional sintering, without any applied pressure (1100°C-15 min). SEM characterizations (see supplementary material S4) revealed the presence of martensite, suggesting that the formation of martensite in the 410L sintered by SPS is not strain-induced.

3.3. Sintering of 316L–410L powder mixtures

3.3.1. Microstructural characterizations

Five powder mixtures containing different 316L/410L mass fractions were prepared (see Table 2). As an example, the core microstructure of the 50-50 blend is shown in Fig. 11. The microstructures of the other sintered powder mixtures are presented in the supplementary material S5. For the five sintered samples, the core-microstructure is composed of equiaxed grains of ferrite and austenite, as confirmed by XRD analyses (PDF 04- 004–6353 and PDF 04-002-1864, respectively; see supplementary material S6). Moreover, a fine lath-shaped microstructure can be observed. It likely corresponds to martensite, compared to the 410L sintered alone. It is known in the literature that the PM elaboration of DSS via the blending of a ferritic and an austenitic powder leads to the formation of a new constituent located at the austenite/ferrite interfaces [11,12,17–20,49,50]. Various denominations have been used to refer to this constituent: interphase [10], interdiffusion zone [16,49,51], and mixed constituent [11,18,50]. However, in the literature, the nature of this interface remains still unclear.

Fig. 12 displays the EBSD phase maps of the five 316L–410L powder mixtures. The identification of martensite was done by using the same

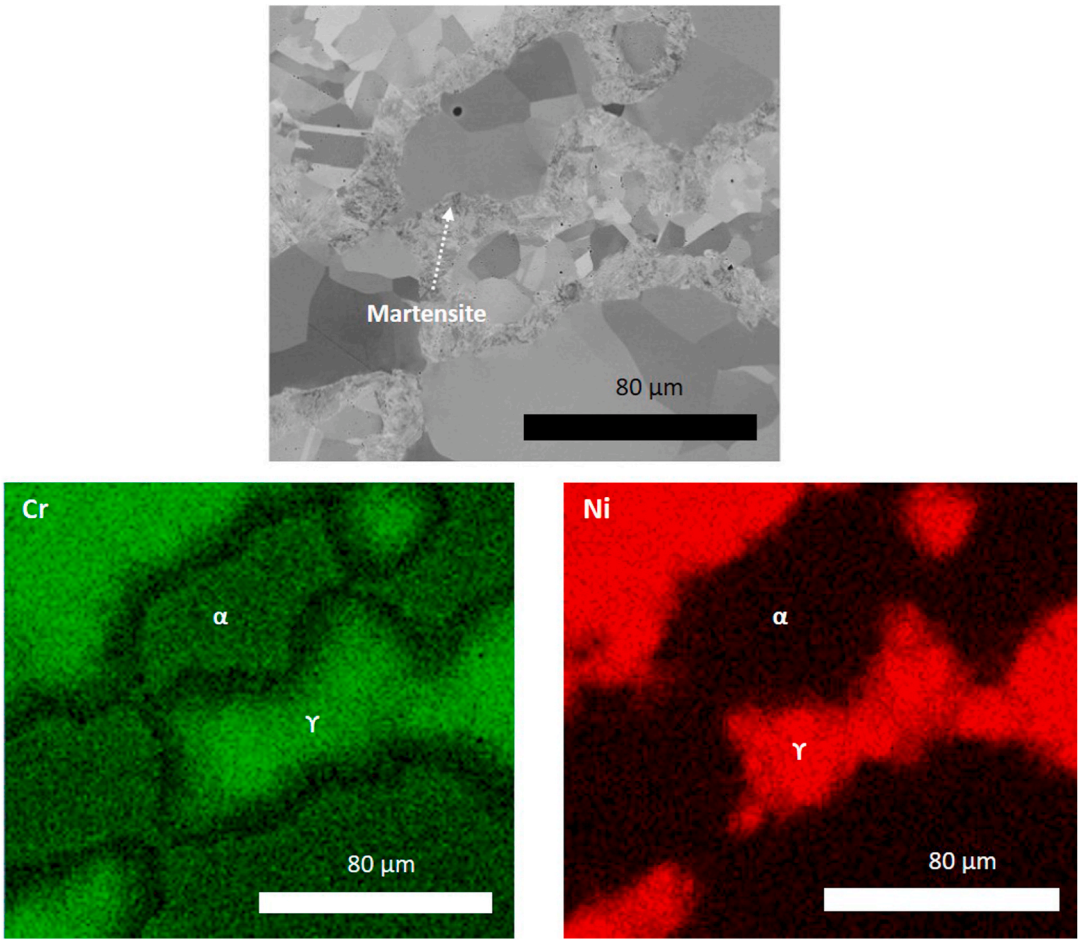

Fig. 13. EDS maps of Cr and Ni in the 50-50 blend.

approach explained for the sintered 410L, based on IQ parameter. Martensite forms preferably at the 316L/410L interfaces and is characterized by a fine microstructure. Further away from the 316L/410L interfaces, large ferritic and austenitic grains can be observed. It is worth noting that under the sintering conditions used in the present study, the starting 410L powder particles strongly deform. On the contrary, the initial 316L powder particles undergo less important deformation and are still observable. The differences in crystal structure and hardness between ferrite and austenite (190 ± 15 HV0.1 and 226 ± 15 HV0.1 respectively, as measured in the present study) may explain the more significant 410L particles deformation. Therefore, this kind of DSS can be defined as a composite, as the characteristic size of both the ferritic and austenitic domains formed after sintering corresponds to the one of the initial powder particles (up to some hundred microns). These domains are composed of equiaxed grains, having a size ranging from some microns to some tens of microns. In contrast, in duplex steels elaborated by conventional methods, the typical size of the austenitic and ferritic domains is smaller, of the order of some tens to one hundred microns, but each domain corresponds to a single grain [52–54].

This "composite effect" has also been mentioned by Villaret et al. [17] in the case of a 50-50 blend of 316L and Fe–9Cr–1Mo sintered by SPS (1100°C-76 MPa-10 min) and HIP (1160°C-102 MPa-180 min). The authors stated that the initial powder particles are visible in the powder mixtures because of the short diffusion time and the absence of a liquid phase, limiting the homogenization of the alloying elements. The ease of deformation and flow of 410L in the blends can be attributed to its b.c.c. structure. Indeed, it intrinsically offers lower resistance compared to the f.c.c. structure of 316L, as also reported in the case of other ferritic powders mixed with 316L and then sintered [12,17–20]. Stavroulakis et al. [19,20] explained that the ferritic powder SA508 has intrinsically a lower flow strength than 316L at high temperatures (1120 °C and 1160 °C). They also pointed out that this reduced strength can be attributed to the lack of alloying elements that contribute to solid solution strengthening. This, in turn, leads to the deformation of SA508, forming a surrounding matrix around 316L particles.

In the 10–90 and 25–75 samples elaborated in the present study (Fig. 12(a) and (b)), it is possible to observe the presence of islands of ferrite surrounded by the austenitic matrix. This "island" effect is less evident in the 50-50 blend (Fig. 12 (c)), because of a more balanced initial mass fraction of 316L and 410L. In the 75-25 and 90-10 mixtures (Fig. 12(d) and (e)), martensite does not only form at the austenite/ferrite interfaces, but also at grain boundaries inside the ferritic regions. This is in agreement with what was observed for the 410L sintered alone. The EBSD orientation maps (see supplementary material S7) display a random grain orientation in the blends and confirm the isotropic natures of the 316L–410L mixtures.

3.3.2. *Diffusion mechanism*

When powder particles of different chemical compositions are in direct contact, diffusion phenomena of elements occur during sintering at the heteromaterial interfaces. In the following of the study, only the 50-50 blend will be considered to investigate the diffusion phenomena leading to the final observed microstructure. The EDS maps illustrating the distribution of Cr and Ni in the 50-50 sample are shown in Fig. 13. Austenite is richer in Ni and Cr and can be easily distinguished from ferrite. Additionally, a decrease of the Cr content is manifest in the martensitic regions between austenite and ferrite.

An EDS line scan (Fig. 14 (a)) was performed from a ferritic to an

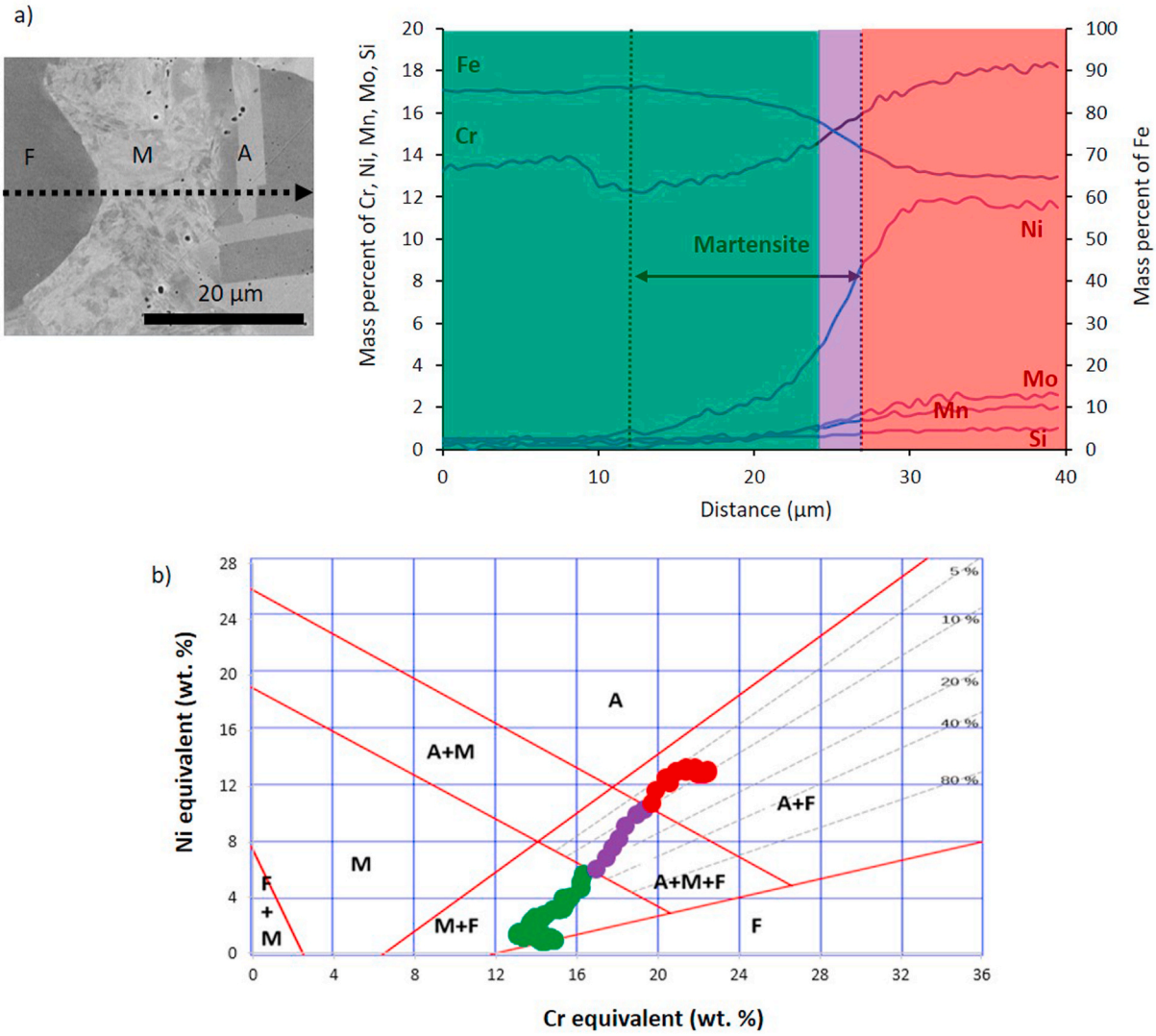

Fig. 14. (a) EDS line scan of the 50-50 blend; (b) Schaeffler diagram.

Table 3
Diffusion coefficient of elements in b.c.c. and f.c.c. phases at 1100 °C (Dictra MOBFE7 database).

D (m^2/s)	b.c.c.	f.c.c.
Cr	$4.72.10^{-13}$	$1.25.10^{-15}$
Ni	$2.67.10^{-13}$	$3.03.10^{-16}$

austenitic region separated by a martensitic zone. The diffusion profiles reveal that Cr, Ni, Mn, Mo, and Si diffuse from austenite (with higher alloying element concentrations) to ferrite. These results are supported by Cr and Ni calculated diffusion coefficients at 1100 °C (Table 3), which are higher in b.c.c. (ferrite and martensite) than in f.c.c. (austenite). This is in agreement also with the values reported by Seki et al. [55]. In contrast, Fe diffuses from ferrite to austenite, due to the higher Fe content in 410L. The Cr diffusion profile exhibits a slight decrease close to the ferrite/martensite interface. This is likely due to the partial austenitization of ferrite during heating, which results in the rejection of Cr. During cooling, a part of austenite transforms into ferrite. At the same time, the remaining austenite transforms into martensite at a lower temperature, following the mechanism already described for the 410L sintered alone.

In addition, EDS profiles revealed that Cr and Ni diffuse over a total length of 26 and 20 µm respectively. This difference can be attributed to the Cr diffusion coefficient, which is roughly twice that of Ni in b.c.c. phases at 1100 °C. The Schaeffler diagram (Fig. 14 (b)) can be used to predict the phases likely to form. This is based on the chromium and nickel equivalent values calculated using the following equations [56]:

$$Cr_{eq} = \text{wt.\% Cr} + \text{wt.\% Mo} + 1.5\ \text{wt\% Si} \quad (3)$$

$$Ni_{eq} = \text{wt.\% Ni} + 30\ \text{wt\% C} + 0.5\ \text{wt\% Mn} \quad (4)$$

The calculated Cr_{eq} and Ni_{eq} along the scan line of Fig. 14 (a) are reported on the Schaeffler diagram of Fig. 14 (b), using the same color code. The varying chemical composition in the martensite region leads to the simultaneous presence of different phases.

- martensite + ferrite + austenite in the areas near the interface with austenite;
- martensite + ferrite near the interface with ferrite.

To better understand the martensite formation mechanism in 316L–410L mixtures, 410L particles were coated with tantalum, subsequently mixed with 316L in equal mass fractions, and sintered by SPS. The resulting sample is denoted 50Ta-50. Ta is employed as a marker to identify the initial interface between 316L and 410L. The microstructure of the 50Ta-50 sample is shown in Fig. 15. Due to Z-contrast, Ta appears

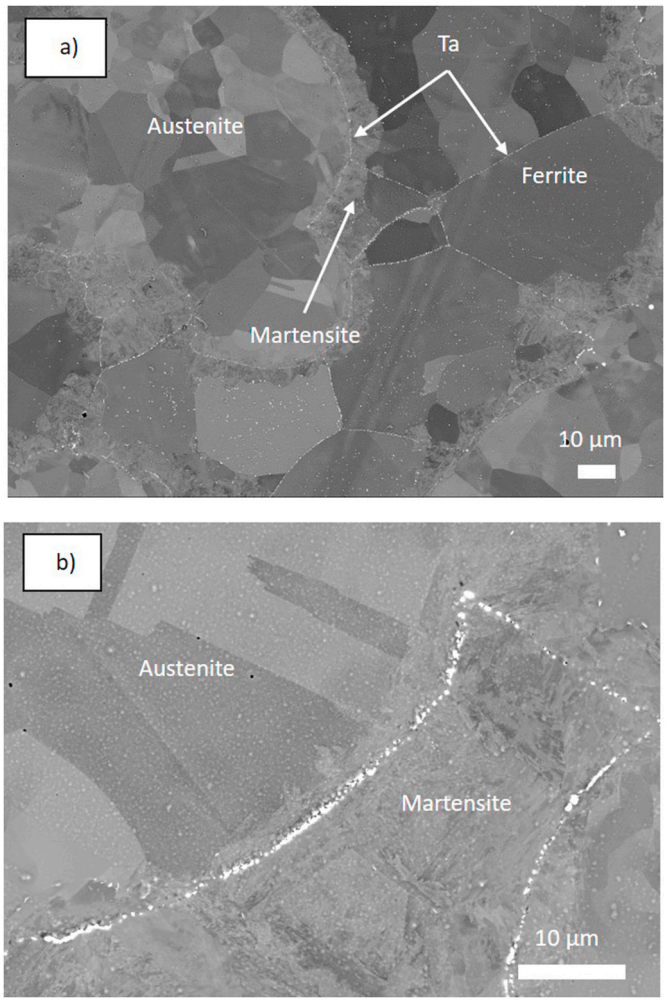

Fig. 15. Core microstructure of 50Ta-50 blend: (a) global view; (b) magnification.

in white in backscattered images. Ta is located either at the junctions of two ferrite grains or at the interfaces between austenite and martensite on the austenite side (Fig. 15 (a). It is worth noting that a martensitic region can be observed close to the initial interface in the 316L particles (Fig. 15 (b)).

EDS line scan of Cr and Ni was performed and overlapped to those of the 50-50 sample (Fig. 16). Ta does not diffuse and has no significant effect on the diffusion of Cr and Ni. The use of Ta as a marker indicates that the martensite formation mechanism at the 316L–410L interfaces can be elucidated as follow.

- In the 410L, austenite forms following the partial austenitization of ferrite. During cooling, a part of the resulting austenite transforms into ferrite and the remaining austenite transforms into martensite at a lower temperature, following the mechanism previously described for the 410L sintered alone.
- In the 316L, austenite undergoes a reduction of Cr and Ni until reaching C_{req} and Ni_{eq} values of 18 and 10 respectively, corresponding to a composition of 16 wt% Cr, 8.9 wt% Ni, 1.7 wt% Mo, 1.4 wt% Mn, and 0.8 wt% Si. This elementary composition leads to the partial transformation of austenite into martensite. This is in agreement with the existence of an A + M + F region in the Schaeffler diagram near the interface between martensite and austenite (Fig. 14 (b)). It is possible to claim that Cr and Ni diffusion influence the total width of the martensitic region.

4. Conclusions

In the present work, duplex stainless steels were elaborated via SPS (1100°C-70 MPa-15 min) by sintering mixtures of 316L and 410L. The originality of this approach is that the characteristic size of the ferritic and austenitic domains in the final sintered material is that of the initial powder particles (up to some hundred microns). These domains are formed by equiaxed isotropic grains, having a size ranging from some microns up to some tens of microns. This microstructure is different from the one observed in duplex steels elaborated by conventional methods. Indeed, in this case, the typical size of the austenitic and ferritic domains is the size of the metallurgical grains (of the order of some tens to one hundred microns).

This particular microstructure justifies the use of the term COMPLEX (i.e. composite duplex stainless steels) to describe the DSS elaborated in the present study. The main findings can be summarized as follow.

- In the case of 410L sintered individually, the heating step induces a partial transformation of ferrite into austenite, with subsequent

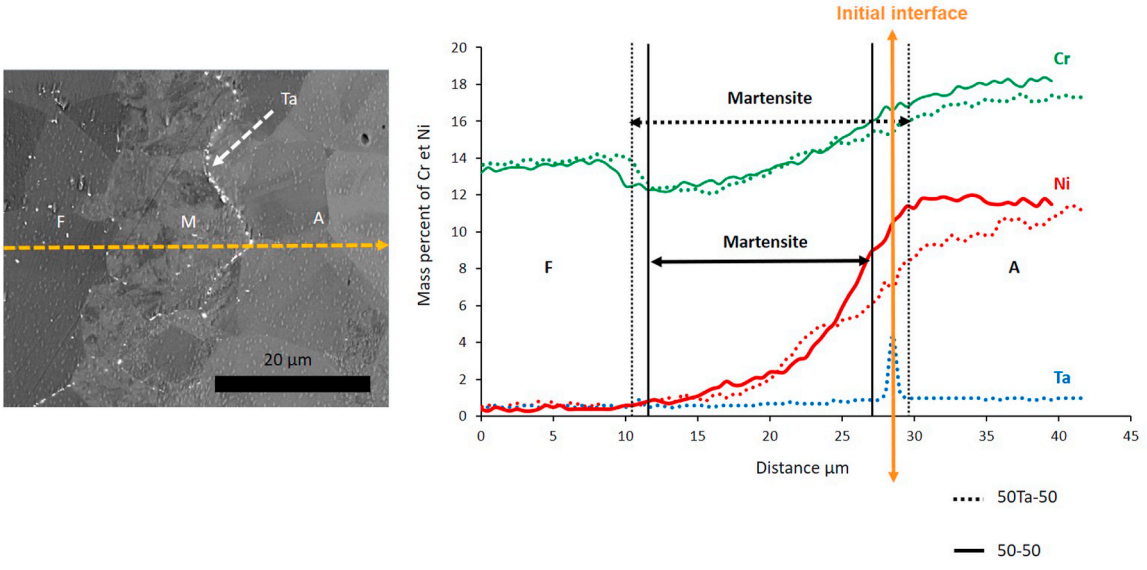

Fig. 16. EDS line scan of 50Ta-50 and 50-50 blends.

rejection of Cr (alphagenic element). During cooling, this austenite transforms firstly into ferrite at about 730 °C, and then into martensite at 350 °C. The formation of martensite is associated with chromium depletion occurring during the partial austenitization of ferrite. Opposite, the 316L sintered individually is fully austenitic;

- In the 316L–410L powder mixtures, the initial powder particles are always visible, because of the short diffusion time and the absence of a liquid phase, limiting the homogenization of elements. During sintering, densification is mainly achieved by the deformation of the 410L particles, as the 316L ones do not undergo noticeable deformation. This may be explained by the differences in crystallographic structure, alloying element amount and hardness between ferrite and austenite.
- Ta marking experiments revealed that in the 316L–410L blends, martensite forms at the austenite/ferrite interfaces mainly in 410L but also in 316L, following two distinct mechanisms. On the 410L side, martensite formation follows the same mechanism as described for individually sintered 410L. On the 316L side, austenite is destabilized due to the diffusion of Cr and Ni towards ferrite. 316L reaches Cr_{eq} and Ni_{eq} concentrations leading to the formation of martensite. Therefore, the width of the martensitic region depends on Cr and Ni diffusion.

CRediT authorship contribution statement

R. Mvodo Eba: Writing – original draft, Validation, Investigation. **M. R. Ardigo-Besnard:** Writing – review & editing, Validation, Supervision, Project administration, Conceptualization. **J.-P. Chateau-Cornu:** Writing – review & editing, Validation, Supervision, Project administration, Conceptualization. **F. Herbst:** Investigation. **N. Geoffroy:** Investigation. **A. Besnard:** Writing – review & editing, Resources, Investigation. **C. Vandenabeele:** Resources, Investigation. **S. Lucas:** Resources, Investigation. **A. Descamps-Mandine:** Investigation. **C. Josse:** Investigation.

Declaration of competing interest

The authors declare the following financial interests/personal relationships which may be considered as potential competing interests.

Maria-Rosa Ardigo-Besnard reports financial support was provided by Bourgogne-Franche-Comte Region. If there are other authors, they declare that they have no known competing financial interests or personal relationships that could have appeared to influence the work reported in this paper.

Data availability

Data will be made available on request.

Acknowledgements

The authors wish to thank the Bourgogne-Franche-Comté Region (project number 2022Y-13808) for their financial support of the THEMPO project, for the FIB and TEM experiments.

Appendix A. Supplementary data

Supplementary data to this article can be found online at https://doi.org/10.1016/j.matchemphys.2024.129796.

References

[1] E.C. Bain, W.E. Griffiths, An introduction to the iron-chromium-nickel alloys, Trans. Aime 75 (1927) 166–211.
[2] R. Gunn, Duplex Stainless Steels: Microstructure, Properties and Applications, Woodhead Publishing, Cambridge, England, 1997.
[3] S.D. Kahar, Duplex stainless steels-an overview, Int. J. Eng. Res. Afr. 7 (2017) 27–36, https://doi.org/10.9790/9622-0704042736.
[4] R. Francis, G. Byrne, Duplex stainless steels-alloys for the 21st century, Metals 11 (2021) 836, https://doi.org/10.3390/met11050836.
[5] M. Liljas, P. Johansson, H. Liu, C.A. Olsson, Development of a lean duplex stainless steel, Steel Res. Int. 79 (2008) 466–473, https://doi.org/10.1002/srin.200806154.
[6] A.B. Outokumpu Stainless, Handbook of Stainless Steel, Avesta Resarch Centre, Avesta, Sweden, 2013. http://www.steel-stainless.org/media/1546/outokumpu-stainless-steel-handbook.pdf.
[7] I. Calliari, E. Ramous, P. Bassani, Phase transformation in duplex stainless steels after isothermal treatments, continuous cooling and cold working, Mater. Sci. Forum 638–642 (2010) 2986–2991. https://doi.org/10.4028/www.scientific.net/MSF.638-642.2986.
[8] J.-O. Nilsson, Super duplex stainless steels, Mater. Sci. Technol. 8 (1992) 685–700, https://doi.org/10.1179/mst.1992.8.8.685.
[9] J. Charles, Super duplex stainless steels: structure and properties, in: Duplex Stainless Steels, Les Editions de Physique, Les Ulis Cedex, France, 1991, pp. 151–168.
[10] J.M. Ruiz-Prieto, W. Moriera, J.M. Torralba, L.E.G. Cambronero, Powder metallurgical duplex austenitic-ferritic stainless steels from prealloyed and mixed powders, Powder, Metall. 37 (1994) 57–60, https://doi.org/10.1179/pom.1994.37.1.57.
[11] T. Marcu Puscas, A. Molinari, J. Kazior, T. Pieczonka, M. Nykiel, Sintering transformations in mixtures of austenitic and ferritic stainless steel powders, Powder, Metall. 44 (2001) 48–52, https://doi.org/10.1179/003258901666167.
[12] A. García-Junceda, M. Rincón, J.M. Torralba, Development of duplex stainless steels by field-assisted hot pressing: influence of the particle size and morphology of the powders on the final mechanical properties, Metall. Mater. Trans A 49 (2018) 264–271, https://doi.org/10.1007/s11661-017-4385-2.
[13] O. Guillon, J. Gonzalez-Julian, B. Dargatz, T. Kessel, G. Schierning, J. Räthel, M. Herrmann, Field-assisted sintering technology/spark plasma sintering: mechanisms, materials, and technology developments, Adv. Eng. Mater. 16 (2014) 830–849, https://doi.org/10.1002/adem.201300409.
[14] L.A. Dobrzański, Z. Brytan, M.A. Grande, M. Rosso, Innovative PM duplex stainless steels obtained basing on the Schaeffler diagram, Arch. Mater. Sci. Eng. 30 (2008) 49–52. https://api.semanticscholar.org/CorpusID:134131286.
[15] R.S. Mahale, V. Shamanth, P.C. Sharath, R. Shashanka, K. Hemanth, A review on spark plasma sintering of duplex stainless steels, Mater. Today: Proc. 45 (2021) 138–144, https://doi.org/10.1016/j.matpr.2020.10.357.
[16] L.A. Dobrzanski, Z. Brytan, M.A. Grande, M. Rosso, Properties of duplex stainless steels made by powder metallurgy, Arch. Mater. Sci. 28 (4) (2007) 217–223. https://api.semanticscholar.org/CorpusID:137374069.
[17] F. Villaret, Y. de Carlan, P. Aubry, D. Fabrègue, J. Garnier, X. Boulnat, Duplex and graded austenitic-to-martensitic steels by powder metallurgy: interface diffusion and strength composite effect, Mater. Sci. Eng. A 882 (2023) 145405, https://doi.org/10.1016/j.msea.2023.145405.
[18] A. García-Junceda, C. Díaz-Rivera, V. Gómez-Torralba, M. Rincón, M. Campos, J. M. Torralba, Analysis of the interface and mechanical properties of field-assisted sintered duplex stainless steels, Mater. Sci. Eng. A 740–741 (2019) 410–419, https://doi.org/10.1016/j.msea.2018.10.111.
[19] E. Stavroulakis, D. Bowden, S. Irukuvarghula, A. Garner, E. Pickering, D. Stewart, M. Preuss, Characterisation of ferritic to austenitic steel functional grading via powder hot isostatic pressing, Mater. Today Commun. 31 (2022) 103442, https://doi.org/10.1016/j.mtcomm.2022.103442.
[20] E. Stavroulakis, S. Irukuvarghula, E. Pickering, D. Stewart, M. Preuss, Fundamental aspects of functional grading via powder hot isostatic pressing - development of microstructure and diffusional processes, Mater. Des. 215 (2022) 110437, https://doi.org/10.1016/j.matdes.2022.110437.
[21] M.R. Ardigo-Besnard, A. Besnard, Y. Pinot, F. Bussière, J.-P. Chateau-Cornu, C. Vandenabeele, S. Lucas, N. Watiez, A. Descamps-Mandine, C. Josse, A. Proietti, Austenitic-to-austenitic-ferritic stainless steel transformation via PVD powder surface functionalization and spark plasma sintering, Mater 33 (2024) 102002, https://doi.org/10.1016/j.mtla.2023.102002.
[22] W.H. Rhodes, Agglomerate and particle size effects on sintering yttria-stabilized zirconia, J. Am. Ceram. Soc. 67 (2) (1981) 19–22, https://doi.org/10.1111/j.1151-2916.1981.tb09552.x.
[23] F. Pengjun, X. Yi, L. Xinggang, C. Ya, Influence of Atomizing Gas and Cooling Rate on solidification characterization of nickel-based superalloy powders, Rare. Met. Mater. Eng. 47 (2018) 423–430, https://doi.org/10.1016/S1875-5372(18)30082-1.
[24] D. Beckers, N. Ellendt, U. Fritsching, V. Uhlenwinkel, Impact of process flow conditions on particle morphology in metal powder production via gas atomization, Adv. Powder Technol. 31 (2020) 300–311, https://doi.org/10.1016/j.apt.2019.10.022.
[25] G.S. Kumar, M. Sateshwar, A.R. Sharma, M. Palit, R. Sarkar, P. Ghosal, G.A. Rao, Particle size dependent microstructure evolution of inert gas atomized nickel base superalloy powders, J. Alloys Compd. 909 (2022) 164772, https://doi.org/10.1016/j.jallcom.2022.164772.
[26] H.F. Fischmeister, A.D. Ozerskii, L. Olsson, Solidification structure of gas-atomized high-speed steel powders, Powder, Metall. 25 (1982) 1–9, https://doi.org/10.1179/pom.1982.25.1.1.
[27] U. Fritsching, Droplets and particles in sprays: tailoring particle properties within spray processes, China Particuol. 3 (2005) 125–133, https://doi.org/10.1016/S1672-2515(07)60178-X.

[28] L. Achelis, V. Uhlenwinkel, Characterisation of metal powders generated by a pressure-gas-atomiser, Mater. Sci. Eng. A 477 (2008) 15–20, https://doi.org/10.1016/j.msea.2007.07.095.
[29] A. Mussatto, R. Groarke, A. O'Neill, M.A. Obeidi, Y. Delaure, D. Brabazon, Influences of powder morphology and spreading parameters on the powder bed topography uniformity in powder bed fusion metal additive manufacturing, Addit. Manuf. 38 (2021) 101807, https://doi.org/10.1016/j.addma.2020.101807.
[30] K. Danjo, K. Kinoshita, K. Kitagawa, K. Iida, H. Sunada, A. Otsuka, Effect of particle shape on the compaction and flow properties of powders, Chem. Pharm. Bull. 37 (1989) 3070–3073, https://doi.org/10.1248/cpb.37.3070.
[31] P. Grgač, M. Behúlová, R. Moravčík, J. Mesárošová, Semi-quantitative model of the microstructure development in the high-alloyed iron based alloy during atomization, Mat. Res. 15 (2012) 705–712, https://doi.org/10.1590/S1516-14392012005000055.
[32] P. Shukla, R.K. Mandal, S.N. Ojha, Non-equilibrium solidification of undercooled droplets during atomization process, Bull. Mater. Sci. 24 (2001) 547–554, https://doi.org/10.1007/BF02706729.
[33] G.S. Kumar, M. Sateshwar, A.R. Sharma, M. Palit, R. Sarkar, P. Ghosal, G.A. Rao, Particle size dependent microstructure evolution of inert gas atomized nickel base superalloy powders, J. Alloys Compd. 909 (2022) 164772, https://doi.org/10.1016/j.jallcom.2022.164772.
[34] G. Marnier, C. Keller, J. Noudem, E. Hug, Functional properties of a spark plasma sintered ultrafine-grained 316L steel, Mater. Des. 63 (2014) 633–640, https://doi.org/10.1016/j.matdes.2014.06.053.
[35] A.B. Kale, A. Bag, J.-H. Hwang, E.G. Castle, M.J. Reece, S.-H. Choi, The deformation and fracture behaviors of 316L stainless steels fabricated by spark plasma sintering technique. under uniaxial tension, Mater. Sci. Eng. A 707 (2017) 362–372, https://doi.org/10.1016/j.msea.2017.09.058.
[36] M.L. Greef, M. Du Toit, Sensitisation of two 11–12% chromium type EN 1.4003 ferritic stainless steels during continuous cooling after welding, Weld. World 50 (2006) 18–27, https://doi.org/10.1007/BF03266532.
[37] M. Dadé, J. Malaplate, J.C. Brachet, T. Guilbert, C. Toffolon-Masclet, Influence of chemical composition on the microstructure and phase transformations of Fe-14Cr ferritic steels, Mater 7 (2019) 100388, https://doi.org/10.1016/j.mtla.2019.100388.
[38] A. Baghdadchi, V.A. Hosseini, L. Karlsson, Identification and quantification of martensite in ferritic-austenitic stainless steels and welds, J. Mater. Res. Technol. 15 (2021) 3610–3621, https://doi.org/10.1016/j.jmrt.2021.09.153.
[39] M.M. Nowell, S.I. Wright, J.O. Carpenter, Differentiating ferrite and martensite in steel microstructures using electron backscatter diffraction, in: Proceedings of the Materials Science and Technology Conference and Exhibition, Pittsburg, Pennsylvania, USA, 2009.
[40] S. Vunnama, A. Saboob, C. Sudbrackb, T.L. Starr, Effect of powder chemical composition on the as-built microstructure of 17-4 PH stainless steel processed by selective laser melting, Addit. Manuf. 30 (2019) 100876, https://doi.org/10.1016/j.addma.2019.100876.
[41] M.A. Auger, V. de Castro, T. Leguey, A. Muñoz, R. Pareja, Microstructure and mechanical behavior of ODS and non-ODS Fe–14Cr model alloys produced by spark plasma sintering, J. Nucl. Mater. 436 (2013) 68–75, https://doi.org/10.1016/j.jnucmat.2013.01.331.
[42] W. Zhai, N. Wu, W. Zhou, Laser metal deposition of low carbon 410L stainless steel and heat treatment, Mater. Sci. Eng. A 872 (2023) 144987, https://doi.org/10.1016/j.msea.2023.144987.
[43] V. Seetharaman, Deformation and martensitic transformation, Bull. Mater. Sci. 6 (1984) 703–716, https://doi.org/10.1007/BF02743999.
[44] T.Y. Hsu, Carbon diffusion and kinetics during the lath martensite formation, J. Phys. IV (5) (1995) 351–354, https://doi.org/10.1051/jp4:1995851.
[45] M.O.H. Amuda, E.T. Akinlabi, S. Mridha, Ferritic Stainless Steels: metallurgy, application and weldability, Ref. Modul. Mater. Sci. Mater. Eng. (2016), https://doi.org/10.1016/B978-0-12-803581-8.04010-8.
[46] M.C. Tsai, C.S. Chiou, J.S. Du, J.R. Yang, Phase transformation in AISI 410 stainless steel, Mater. Sci. Eng. A 332 (2002) 1–10, https://doi.org/10.1016/S0921-5093(01)01710-5.
[47] V. Raghavan, D.P. Antia, The driving force for martensitic transformations in low alloy steels, Metall. Mater. Trans. A 27 (1996) 1127–1132, https://doi.org/10.1007/BF02649781.
[48] S. Zheng, Q. Wu, Q. Huang, S. Liu, Y. Han, Influence of different cooling rates on the microstructure of the HAZ and welding CCT diagram of CLAM steel, Fusion Eng. Des. 86 (2011) 2616–2619, https://doi.org/10.1016/j.fusengdes.2011.02.072.
[49] M. Campos, A. Bautista, D. Cáceres, J. Abenojar, J.M. Torralba, Study of the interfaces between austenite and ferrite grains in P/M duplex stainless steels, J. Eur. Ceram. Soc. 23 (2003) 2813–2819, https://doi.org/10.1016/S0955-2219(03)00293-0.
[50] F. Martín, C. García, Y. Blanco, M.L. Rodriguez-Mendez, Influence of sinter-cooling rate on the mechanical properties of powder metallurgy austenitic, ferritic, and duplex stainless steels sintered in vacuum, Mater. Sci. Eng. A 642 (2015) 360–365, https://doi.org/10.1016/j.msea.2015.06.097.
[51] C.J. Múnez, M.V. Utrilla, A. Ureña, Effect of temperature on sintered austeno-ferritic stainless steel microstructure, J. Alloys Compd. 463 (2008) 552–558, https://doi.org/10.1016/j.jallcom.2007.09.107.
[52] Z. Liu, Y. Han, Z. Wu, J. Sun, G. Zu, W. Zhu, X. Ran, Microstructures and mechanical properties of cold-rolled 21Cr lean duplex stainless steel with medium to high cold rolling reductions, Mater. Today Commun. 33 (2022) 104860, https://doi.org/10.1016/j.mtcomm.2022.104860.
[53] Y. Zhang, Q. Zhang, Y. Wang, X. Wang, Effect of microstructure tailoring on the deformation coordination of welded duplex stainless steel, Mater. Charact 195 (2023) 112555, https://doi.org/10.1016/j.matchar.2022.112555.
[54] J. Michalska, B. Chmiela, Phase analysis in duplex stainless steel: comparison of EBSD and quantitative metallography methods, IOP Conf. Series: Mater. Sci. Eng. 55 (2014) 012010, https://doi.org/10.1088/1757-899X/55/1/012010.
[55] A. Seki, K. Ogawa, T. Nishibata, Analysis of diffusion-controlled phenomena at the interface of α/γ diffusion couples of stainless steels, ISIJ Int. 53 (2013) 2242–2249, https://doi.org/10.2355/isijinternational.53.2242.
[56] P. Guiraldenq, O.H. Duparc, The genesis of the Schaeffler diagram in the history of stainless steel, Metall. Res. Technol. 114 (2017) 613, https://doi.org/10.1051/metal/2017059.